



Article

Scattering Properties of Non-Gaussian Ocean Surface with the SSA Model Applied to GNSS-R

Weichen Sun ^{1,2,3}, Xiaochen Wang ^{1,2,*}, Bing Han ^{1,2}, Dadi Meng ^{1,2} and Wei Wan ⁴

¹ Aerospace Information Research Institute, Chinese Academy of Sciences, Beijing 100094, China; sunweichen21@mails.ucas.ac.cn (W.S.)

² Key Laboratory of Technology in Geo-Spatial Information Processing and Application System, Chinese Academy of Sciences, Beijing 100094, China

³ School of Electronic, Electrical and Communication Engineering, University of Chinese Academy of Sciences, Beijing 100049, China

⁴ Institute of Remote Sensing and GIS, School of Earth and Space Sciences, Peking University, Beijing 100871, China

* Correspondence: wangxc@aircas.ac.cn

Abstract: Global Navigation Satellite System Reflectometry (GNSS-R) is an emerging earth observation method for remote sensing of feature parameters using reflected signals from navigation satellites, and is a purely specular bistatic forward scattering observation means with special right-handed circular polarization incident wave. In this paper, the small-slope approximation model of non-Gaussian sea surface is used as the basis to construct the scattering model for the observation geometry of GNSS-R as well as the L-band characteristics, and the fully-polarization normalized bistatic radar scattering cross section (NBRCS) are simulated by the method of polarization synthesis to analyze the scattering characteristics under different wind speeds and directions on the ocean surface, which highlights the variation of NBRCS with wind direction, and the scattering modeling accuracy is improved by comparing with the data of CYGNSS. In addition, we adopt the observation geometry deviating from purely specular geometry, discuss the scattering azimuth angle, scattering influence, and the relative relationship between different polarizations of the scattering angle under the non-specular geometry.

Keywords: non-Gaussian ocean surface; bistatic scattering; global navigation satellite system reflectometry (GNSS-R); ocean wind



Citation: Sun, W.; Wang, X.; Han, B.; Meng, D.; Wan, W. Scattering Properties of Non-Gaussian Ocean Surface with the SSA Model Applied to GNSS-R. *Remote Sens.* **2023**, *15*, 3526. <https://doi.org/10.3390/rs15143526>

Academic Editors: Martin Gade and Yukiharu Hisaki

Received: 16 April 2023

Revised: 25 June 2023

Accepted: 8 July 2023

Published: 13 July 2023



Copyright: © 2023 by the authors. Licensee MDPI, Basel, Switzerland. This article is an open access article distributed under the terms and conditions of the Creative Commons Attribution (CC BY) license (<https://creativecommons.org/licenses/by/4.0/>).

1. Introduction

The Global Navigation Satellite System reflectometer (GNSS-R) is a new type of remote sensing means by using GNSS as a signal source and receiving its L-band signal reflected back from the ground, which can be seen as a bistatic radar observation mode with high temporal resolution using only deployed receivers. After years of research, GNSS-R has gradually developed from ground- and air-based observations to satellite-based observations, and has unique features as well as good performance in the inversion problems of a variety of geographical parameters, e.g., ocean surface wind speed [1–5], wind direction [6–10], ocean surface oil spill [11–13], ocean surface altimetry [14,15], sea ice detection [16], sea ice classification [17], and sea ice altimetry and thickness [18,19]. In recent years, several GNSS-R receiver satellites have been launched into low Earth orbit to receive reflected signals from GNSS systems, including GPS, BeiDou, and Galileo, among which the most symbolic are TechDemoSat-1 (TDS-1) launched by the UK in 2014 [20], Cyclone Global Navigation Satellite System (CYGNSS) launched by NASA in 2016 [21], and the BF-1A/B and FengYun-3E (FY3E) launched by China after 2019 [22], to provide data to aid and advance research in this field.

However, the practical use of the GNSS-R satellites described above is mainly for detecting wind speed at the ocean surface, with polarization in a single form. Unlike

airborne GNSS-R, where the resolution of the data is substantially reduced due to the higher altitude of the satellite receiver and the signal being more severely attenuated as the transmission distance becomes longer, only the signal near the specular reflection point has a higher quality and can be used for the detection of geographic parameters. The application of satellite-based GNSS-R for sea surface detection is mainly in the form of finding relevant characteristic quantities of elements such as wind speed in the vicinity of the specular point (SP) from the Delay Doppler Maps (DDMs), particularly the sea surface normalized bistatic radar scattering cross section (NBRCS) at the SP, which has been shown to be more effective in retrieving wind speeds [23]. Its initial analysis was based on the Kirchhoff approximation in the geometricoptics (KA-GO) modal, which treats the geometry of GNSS-R as pure specular scattering in the forward direction, estimated from the reflected waveform or DDMs [23–26]. Although it shows some robustness in retrieval algorithm of wind speed, this estimation approach leaves it with some inescapable problems in terms of truth value as well as accuracy [27]. In addition, since the polarization characteristics of electromagnetic waves are influenced by factors such as the dielectric constant of the sea surface and geometry, the study of the polarization characteristics of GNSS-R is beneficial for its subsequent application development [28,29], such as wind direction retrieval [30,31].

To solve the above problem, Zavorotny et al. used the small slope approximation (SSA) model to determine the range of incidence angles to which the KA-GO applies. For large incidence angles, the NBRCS calculated by the KA-GO model has some bias, which also affects the quality control problem of the data [32–34]. Modeled with a complex real rough sea surface containing wind and swell waves, the DDMs generated by Clarizia et al. have distinct features that differ from those generated by the Z-V model [24], but the distribution of scattered power is similar to that of the UK -DMC measured results, indicating that the KA-GO alone and the Elfouhaily wave spectrum cannot accurately describe the real scattering characteristics of GNSS-R. Moreover, the KA-GO alone can only give the polarization characteristics of large scale rough surfaces, and if full polarization characteristics need to be considered, the scattering effects in small scale rough surfaces also needs to be considered [31]. The full polarization NBRCS was simulated using the IEM model and the polarization ratios of the left and right circular polarization were found to be insensitive to the ocean wind, and also that the IEM calculations are more complex and require some parallelization [30,35]. Ahmad et al. used the SSA-1 model to predict the full polarization characteristics of L-band sea surface scattering in the bistatic case. The SSA model takes into account the multiple scattering effects from wave breaking and the calculation is more efficient compared to the IEM model, and the small slope approximation (SSA) model is widely used in modeling electromagnetic scattering from rough sea surfaces [36]. However, to improve the accuracy of the cross-polarization, the SSA-2 model was used to calculate the full polarization scattering coefficient for the bistatic case, taking into account surface Bragg scattering, and it was found that the change in wind direction had little effect on the NBRCS for the circular polarization case and that there was still ambiguity and symmetry in the up/down or crosswind direction, but that there was some sensitivity to wind direction if the bistatically scattered signal is received in a non-pure specular direction [37].

All of the above are explorations of improvements in the scattering mechanism of GNSS-R from a scattering model perspective, but the description of the rough sea surface is also very important in this process. Most studies are based on the general Elfouhaily wave spectrum [38], but the use of the Elfouhaily wave spectrum is limited at high wind speeds (25–30 m/s) [27]. On this basis, the sea surface height undulation is generally regarded as a Gaussian stochastic process, and several approximations are made to simplify the calculation process. However, the non-linear wave–wave interactions at the sea surface make the sea surface fluctuations appear non-sinusoidal in shape, thus deviating the sea surface from a Gaussian distribution. The earliest study of electromagnetic scattering from non-Gaussian rough surfaces was carried out by Beckmkn et al. who demonstrated that the non-Gaussian distribution was more consistent with actual sea surface scenarios [39]. To understand the sea surface scattering characteristics under different wind fields, a more

precise description of the sea surface height undulation is required. Cox, Munk et al. measured the sea surface slope distribution by aerial photography of sea surface solar flares, proposed a non-Gaussian distribution of the sea surface slope Cox–Munk Probability Density Function (PDF), defined the skew and peak properties, and modeled the distribution function according to the probability density distribution of the resulting measured slope, which can be expanded on a Gram–Charlier series [40]. The directionality of its slope is described by third-order skewness, while the kurtosis uses fourth-order kurtosis; for the effect of higher-order corrections, one can refer to Refs. [41,42]. Nickolae et al. found that a non-Gaussian distribution of sea surface height undulations can cause an asymmetry in sea surface electromagnetic scattering in upwind and downwind directions [43]. For GNSS-R applications, initially, Estel et al. proposed a new algorithm to extract the sea surface slope PDF from the sea surface reflected GNSS signal from the KA-GO model using airborne experimental data to detect the ocean wind from the perspective of the sea surface slope PDF, and found that the inverse-performed PDF is non-Gaussian without presetting the shape distribution of the PDF, which can effectively solve the 180° ambiguity problem of wind direction detection [6]. However, due to the resolution of the spaceborne data, most studies now focus on the NRBCS amplitude characteristics of SP and explore the scattering characteristics of the scattering point in conjunction with electromagnetic scattering models. Chen et al. modeled a non-Gaussian distributed rough surface in conjunction with an IEM model and introduced a third-order skewness statistic in the case of backward scattering [44]. Later, Bourlier extended the non-Gaussian correction to a fourth-order statistic and explored the scattering properties of the higher frequency band C-band and Ku-band in conjunction with the SSA-1 model, expanding the NRBCS to a uniform Fourier series that better fits the actual sea surface scenario [45]. However, in the lower L-band and in the direction of forward scattering it remains to be discussed. Combining the non-Gaussian correction with the KA-GO model under the GNSS-R geometry, it was found that the effect of wind direction in the purely specular geometry is still very small. This may be constrained by the scattering model and the estimated location of the SP, and the SSA model reflects a different performance from the KA-GO model. Furthermore, if we want to explore the effects of wind direction, we need to look away from purely specular points [46].

According to the above, the key issues with electromagnetic scattering modeling applied to GNSS-R are the lack of studies of the non-Gaussian statistical characteristics of the sea surface at longer wavelengths of L-band radiation and the omission of the full polarization properties of the GNSS circularly polarized signals scattered off a wind-driven ocean.

In this paper, due to the response characteristics of the non-Gaussian distribution to the ocean wind [6], the non-Gaussian sea surface SSA model will be applied to the longer wavelength GNSS-R L-band as well as to the forward scattering geometry [45]. We start with a statistical description of the non-Gaussian sea surface based on the Elfouhaily wave spectrum, based on the L-band characteristics, combined with a non-Gaussian Cox–Munk surface slope probability density function [40]. Secondly, the GNSS-R polarization characteristics under different wind fields and scattering geometries are explored in conjunction with the SSA scattering model and the polarization synthesis method, and compared with CYGNSS data to analyze the accuracy and validity of the true values. Finally, the sensitivity of NRBCS to sea surface wind direction under different scattering geometries is discussed.

2. Materials and Methods

2.1. Data

The Cyclone Global Navigation Satellite System (CYGNSS) is a GNSS-R mission launched by NASA in 2016, with eight co-orbital receiving satellites operating at an altitude of approximately 510 km throughout the mission, one of which can simultaneously receive the reflected point signals from four GPS subsatellites on the Earth's surface. Its mission is mainly to monitor the wind speed at the sea surface, and there are three levels of data

that will be made available to the general public, which we can find in NASA's Physical Oceanography Distributed Active Archive Center (PO. DAAC) on <https://podaac.jpl.nasa.gov/CYGNSS> (accessed on 1 June 2023) [21]. In this study, we use the level 1 V3.1 product on 14 September 2018. Because the specular point passes through the hurricane area during this period, it facilitates the analysis of high wind speed data [47,48].

We use level 1A data to calculate NBRCS, and then matched the NBRCS with ECMWF data. ECMWF data provides hourly information on the ocean wind speed, wind direction, atmosphere, etc., from 1979. It can be downloaded from Copernicus climate change service (C3S) climate database <https://cds.climate.copernicus.eu/cdsapp#!/home> (accessed on 1 June 2023). However, the spatial resolution of wind speed products is different from CYGNSS, so it is essential to match them using temporal-spatial interpolation [3,49].

2.2. Geometry

The scattering geometry of GNSS-R is a specular forward scattering pattern, and from the position of the transmitter and receiver, the specular points on the sea surface can be deduced.

Figure 1 represents the scattering geometry of GNSS-R at any point on the ocean surface. At the specular point, the scattering angle θ_s is equal to the incident angle θ_i , and the same applies to the scattering and incident azimuth angles ($\varphi_s = \varphi_i$). Define the plane of the incident wave as the $\hat{y} - \hat{z}$, we then have $\varphi_s = \varphi_i = 0$. θ_i is in the range of $[0^\circ, 90^\circ]$, and φ_s is in the range of $[0^\circ, 360^\circ]$.

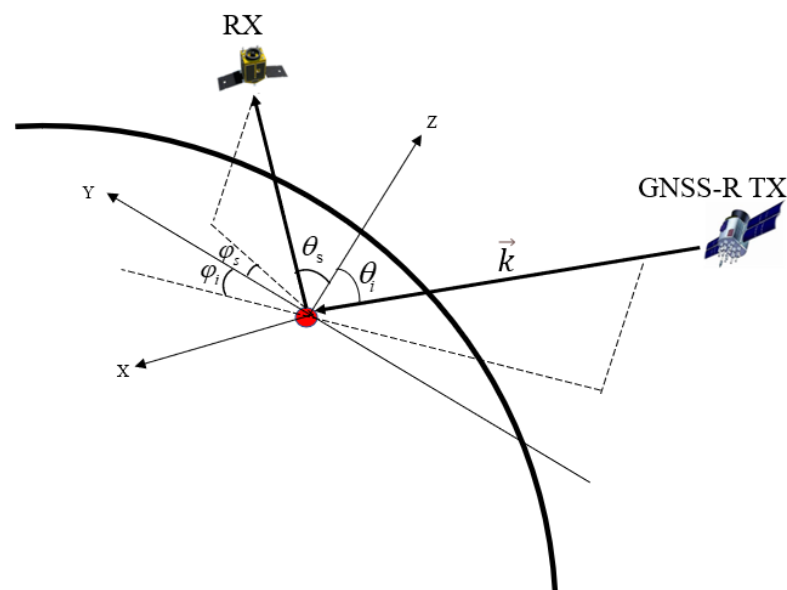


Figure 1. GNSS-R bistatic forward scattering geometry.

Other points around the specular point are also reflected in the DDM depending on their delay as well as their Doppler properties, and their scattering geometry will deviate from the purely specular geometry, and this difference becomes greater the further away from the specular point.

2.3. Polarization Synthesis

Since the GNSS signal source is polarized in right-hand circular polarization, after the reflection from the sea surface, the satellite-borne GNSS-R is now received in left-hand circular polarization. Considering the practical application of GNSS-R, if accurate phase information is to be obtained, only fully polarized reception is possible, that is, to obtain a bistatic radar scattering cross section with dual circular polarization, and linear (horizontal and vertical) polarization (σ_{RR}^0 , σ_{RL}^0 , σ_{RH}^0 and σ_{RV}^0).

S represents the scattering matrix, which can effectively describe the polarization characteristics of the incident and reflected electromagnetic waves.

$$S = \begin{bmatrix} S_{HH} & S_{HV} \\ S_{VH} & S_{VV} \end{bmatrix} \quad (1)$$

The two subscripts of S indicate the polarization of the incident and scattered waves, respectively. H and V indicates horizontal and vertical polarization, respectively.

Under the assumption of scattering reciprocity, the S_{HV} is equal to the S_{VH} . Thus, the fully polarized scattering amplitude in the right-hand circularly polarized incidence mode can be obtained based on the method of polarization synthesis [28,46,50].

$$S_{RH} = \frac{1}{\sqrt{2}}(S_{HH} - iS_{HV}) \quad (2)$$

$$S_{RV} = \frac{1}{\sqrt{2}}(-iS_{VV} + S_{HV}) \quad (3)$$

$$S_{RL} = \frac{1}{2}(S_{HH} - S_{VV} + iS_{VH} + iS_{HV}) \quad (4)$$

$$S_{RR} = \frac{1}{2}(S_{HH} + S_{VV} + iS_{VH} - iS_{HV}) \quad (5)$$

where R and L indicates right- and left-handed circular polarization, respectively.

The relationship between the scattering matrix elements and the BRCS can be expressed as:

$$\sigma_{pq}^0 = \langle S_{pq} S_{pq}^* \rangle \quad (6)$$

where $*$ is the conjugate calculation.

To simplify the calculations, the calculation of the constant coefficients is ignored here and has no effect on the trend of the NBRCS. Thus, in combination with Equations (2)–(5), the fully polarized NBRCS (σ_{RR} , σ_{RL} , σ_{RH} and σ_{RV}) can be described as:

$$\sigma_{RH}^0 = \frac{1}{2} [\sigma_{HH}^0 + \sigma_{HV}^0 - 2\Re(S_{HH} \cdot S_{HV}^*)] \quad (7)$$

$$\sigma_{RV}^0 = \frac{1}{2} [\sigma_{VV}^0 + \sigma_{HV}^0 - 2\Re(S_{VV} \cdot S_{HV}^*)] \quad (8)$$

$$\sigma_{RL}^0 = \frac{1}{4} \left[\sigma_{HH}^0 + \sigma_{VV}^0 + 2\sigma_{HV}^0 - 2\Re(S_{HH} \cdot S_{VV}^* - S_{HV} \cdot S_{VH}^*) \right. \\ \left. + 2\Im(S_{HH} \cdot S_{HV}^* + S_{HH} \cdot S_{VH}^* - S_{VV} \cdot S_{HV}^* - S_{VV} \cdot S_{VH}^*) \right] \quad (9)$$

$$\sigma_{RR}^0 = \frac{1}{4} \left[\sigma_{HH}^0 + \sigma_{VV}^0 + 2\sigma_{HV}^0 + 2\Re(S_{HH} \cdot S_{VV}^* - S_{HV} \cdot S_{VH}^*) \right. \\ \left. - 2\Im(S_{HH} \cdot S_{HV}^* - S_{HH} \cdot S_{VH}^* + S_{VV} \cdot S_{HV}^* - S_{VV} \cdot S_{VH}^*) \right] \quad (10)$$

where \Re and \Im denote the real and imaginary parts of a complex number, respectively.

3. Scattering of Non-Gaussian Ocean Surface

3.1. Scattering Model

Under the influence of different surface winds, the roughness of the sea surface varies. As the roughness of the sea surface increases, the coherent component of specular scattering decreases and the incoherent component of diffuse scattering increases. The KA-GO model cannot accurately reflect the scattering from the sea surface, while the Small Slope Approximation (SSA) model is an approximate representation of the scattering amplitude from a rough surface in the form of a series expansion about the slope of the rough surface, which can describe the scattering contributions from large-, medium-, and small-scale rough surfaces simultaneously [32,51,52].

Bistatic small slope approximation scattering amplitudes of first order for different polarization forms can be expressed as:

$$S_{pq}(\bar{k}_i, \bar{k}_s) = \frac{1}{(2\pi)^2} \frac{2(q_i q_s)^{1/2}}{q_i + q_s} B_{pq}(\bar{k}_i, \bar{k}_s) \cdot \int \exp[-i(\bar{k}_s - \bar{k}_i) \cdot \bar{r} - i(q_i + q_s)z(\bar{r})] d\bar{r} \quad (11)$$

with

$$\bar{k}_i = K \sin \theta_i \hat{k}_i \quad \bar{k}_s = K \sin \theta_s \hat{k}_s \quad (12)$$

$$q_i = K \cos \theta_i \quad q_s = K \cos \theta_s \quad (13)$$

where the subscripts p and q indicate the polarization of the incident and scattered waves, respectively, which can be V and H , $B_{pq}(\bar{k}_i, \bar{k}_s)$ is a matrix of first-order coefficients with respect to the geometric state and polarization mode of the incident and scattered waves, as expressed in Ref. [33]. K is the incident wavenumber, q_i and q_s indicates the projection of the incident and scattered waves in the vertical direction. \bar{k}_i and \bar{k}_s denotes projection on the horizontal plane, \hat{k}_i and \hat{k}_s is its unit vector. z is the height of the sea surface fluctuation.

Substituting Equation (11) into (6), after derivation, the NBRCS for different combinations of polarization ($S_{pq} \cdot S_{p'q'}^* = \sigma_{pp'q'q'}^0$) can be obtained as follows:

$$\sigma_{pp'q'q'}^0(\bar{k}_i, \bar{k}_s) = \frac{1}{\pi} \left| \frac{2q_i q_s}{q_i + q_s} \right|^2 B_{pq}(\bar{k}_i, \bar{k}_s) B_{p'q'}(\bar{k}_i, \bar{k}_s) \cdot \int \exp[-i(\bar{k}_s - \bar{k}_i) \cdot \bar{r}] \cdot \langle \exp[i(q_i + q_s)(z_2 - z_1)] \rangle d\bar{r} \quad (14)$$

where $\langle \exp[i(q_i + q_s)(z_2 - z_1)] \rangle$ is the ensemble average of the difference in height between any two arbitrary points on the sea surface, which is calculated in relation to the statistical method of random sea height.

The non-Gaussian nature of the rough sea surface is caused by non-linear wave-wave interactions and tilt effects, giving a non-sinusoidal trend to the sea surface. It is essential that this feature is not ignored in the calculations.

The third-order statistical moments (skewness) and the fourth-order statistical moments (peakedness) of sea surface undulations are statistics of non-sinusoidal trends. A non-Gaussian correction to the sea surface description is therefore made by adding peakedness and skewness factors to the Gaussian distribution. The skewness correction theoretically distinguishes between up/downwind directions, while the peakedness correction corrects for the absolute value of the scattering cross section. Therefore, the ensemble average in Equation (14) when considering non-Gaussian effects at the sea surface can be expressed as [45,53]:

$$\langle \exp[i(q_i + q_s)(z_2 - z_1)] \rangle \approx \exp[-(q_i + q_s)^2 (\sigma_z^2 - W_2)] \cdot \exp \left\{ -i(q_i + q_s)^3 W_3 + (q_i + q_s)^4 \frac{W_{4d}}{2} \right\} \quad (15)$$

where the first exponential term on the right-hand side of the equation represents the effect of a sea surface height undulation satisfying a Gaussian process, and the second exponential term represents a non-Gaussian correction process. W_2 is the correlation function for sea surface height. W_3 is the skewness factor. $W_{4d} = W_4 - (\sigma_z^2 - W_2)^2$ is a function that measures the deviation of the peakedness factor between non-Gaussian and Gaussian surfaces. W_4 is the peakedness factor. σ_z^2 is the root mean square height of the sea surface, which can be calculated from the wave spectrum.

$$\sigma_z^2 = \int_0^\infty \int_{-\pi}^\pi W(k, \varphi) k dk d\varphi = \int_0^\infty S(k) dk \quad (16)$$

where (k, φ) means the wavenumber and the angle between the direction of wave propagation and the wind direction. $S(k)$ denotes the non-directional spectrum, representing the isotropic part of the sea spectrum. $W(k, \varphi)$ is directional spectrum, which can be expressed as the product of non-directional spectrum and the spreading function $\Phi(k, \varphi)$.

$$W(k, \varphi) = S(k) \cdot \Phi(k, \varphi) \quad (17)$$

3.2. Derivation of Non-Gaussian Statistics

In this section we want to show that the statistical properties of the non-Gaussian ocean surface are strongly dependent on the ocean wind, the incident wave number, and the observation geometry. To provide an accurate description of the ocean surface, Elfouhaily spectrum was chosen for modeling, which considers longer and shorter gravity waves and parasitic capillary waves on the sea surface, respectively, and takes into account the effect of wind zones on the waves, is widely used for modelling scattering from rough sea surfaces, and its definition as well as its calculation can be found in Ref. [38].

Since Equation (16) is calculated by integrating the wave spectrum over the full wave range, the mean square height obtained represents the mean square height of all waves at the sea surface. However, during microwave scattering at the sea surface, not all wavelengths of waves interact with the incident electromagnetic waves and thus contribute to the energy of forward scattering. Since the GNSS signal in the L-band ($f = 1.57$ GHz) will not be sensitive to rough surfaces at all scales, rough surfaces with too high a wave number and too short a wavelength, will not contribute to the roughness measured in the L-band and therefore the wavenumber integral has to be cut off.

In order to determine the appropriate L-band cutoff wavenumber K_c , a method of calculating the cutoff wavenumber in relation to the sea surface wind speed was used, based on the results of NBRCS fitting of aircraft experimental data to GPS signals [54].

$$K_c = \frac{K}{7.5} \cdot \cos\theta_i \cdot \left(1 + \frac{U_{10}}{20}\right) \quad (18)$$

Figure 2 shows the Elfouhaily non-directional spectrum in the wind speed range of 3–18 m/s. The two vertical lines in the figure indicate the wavenumber K , and cutoff wavenumber K_c corresponding to L-band 1.57 GHz. Thus, the integration interval of the σ_z^2 is $[0, K_c]$. Figure 3 shows the variation of the cutoff wavenumber and the mean square height of the sea surface with wind speed, both of which tend to increase as the wind speed becomes higher.

Correlation function W_2 is expressed as a two-dimensional Fourier transform of the wave spectrum, which in polar coordinates $\vec{r} = (r \cos \phi, r \sin \phi)$ can be defined as:

$$W_2(r, \phi) = \int_0^\infty \int_0^{2\pi} W(k, \varphi) \exp[ikr \cos(\phi - \varphi)] k dk d\varphi \quad (19)$$

Taking into account the various anisotropies and combining the Elfouhaily wave spectrum, according to Ref. [45], the correlation function can be simplified and expanded as:

$$W_2(r, \phi) = W_{20}(r) - W_{22}(r) \cos(2\phi) \quad (20)$$

with

$$\begin{cases} W_{20}(r) = \int_0^\infty S(k) J_0(kr) dk \\ W_{22}(r) = \int_0^\infty S(k) J_2(kr) \Delta(k) dk \end{cases} \quad (21)$$

where $W_{20}(r)$ is the isotropic part and $W_{22}(r)$ is the anisotropic part. $\Delta(k)$ is the spreading function. J_n is the n th-order Bessel function of the first kind.

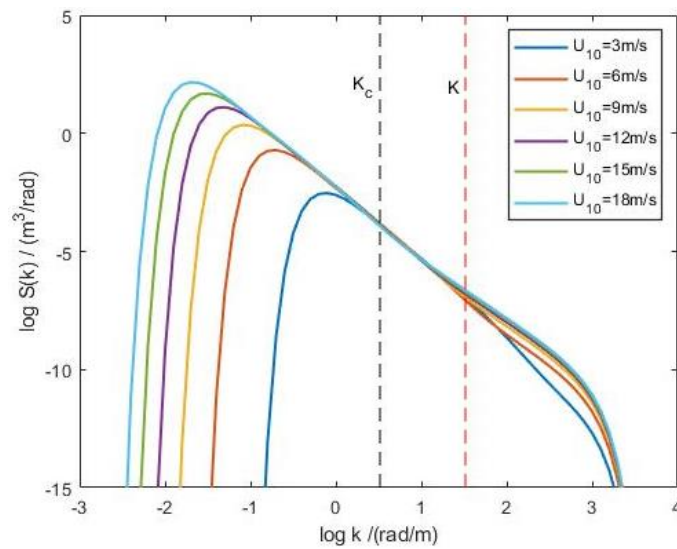


Figure 2. The Elfouhaily non-directional spectrum in the wind speed range of 3–18 m/s. K is the wavenumber corresponding to 1.57 GHz.

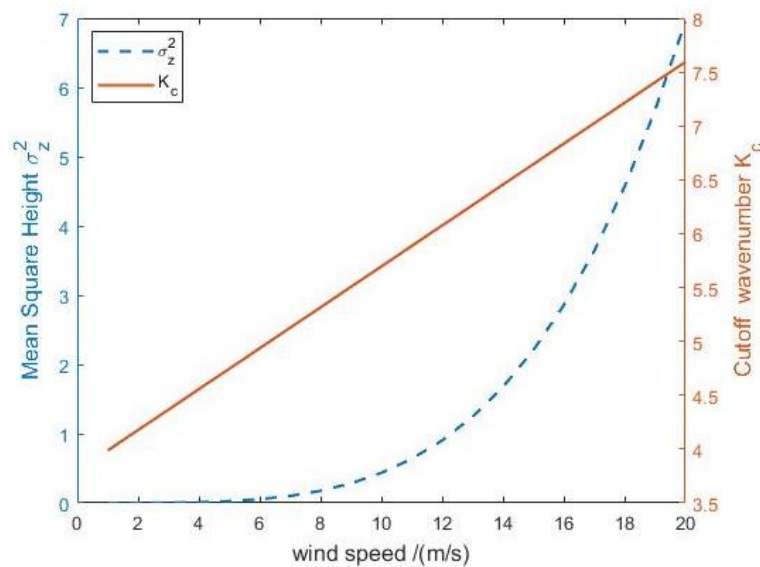


Figure 3. Trends in cutoff wavenumber and sea surface mean square height with wind speed. Blue dashed line indicates the mean square height σ_z^2 . Red solid line indicates the cutoff wavenumber K_c .

Figure 4 shows the normalized correlation function based on the Elfouhaily wave spectrum in different wind speed. As the wind speed increases, the correlation length of the sea surface height becomes larger and, the correlation function captures the asymmetry between up/crosswind directions, however, the asymmetry between up/downwind directions is not captured and there is some ambiguity, which is due to the effect of $\cos(2\phi)$. In addition, due to the multiscale character of the sea surface, its correlation function appears to have both positive and negative components. Theoretically, the addition of higher order statistics through non-Gaussian corrections could distinguish such wind direction differences in scattering modeling. However, the peakedness and skewness factors cannot be obtained directly from the wave spectrum function and need to be derived from the PDF of the total sea surface slope.

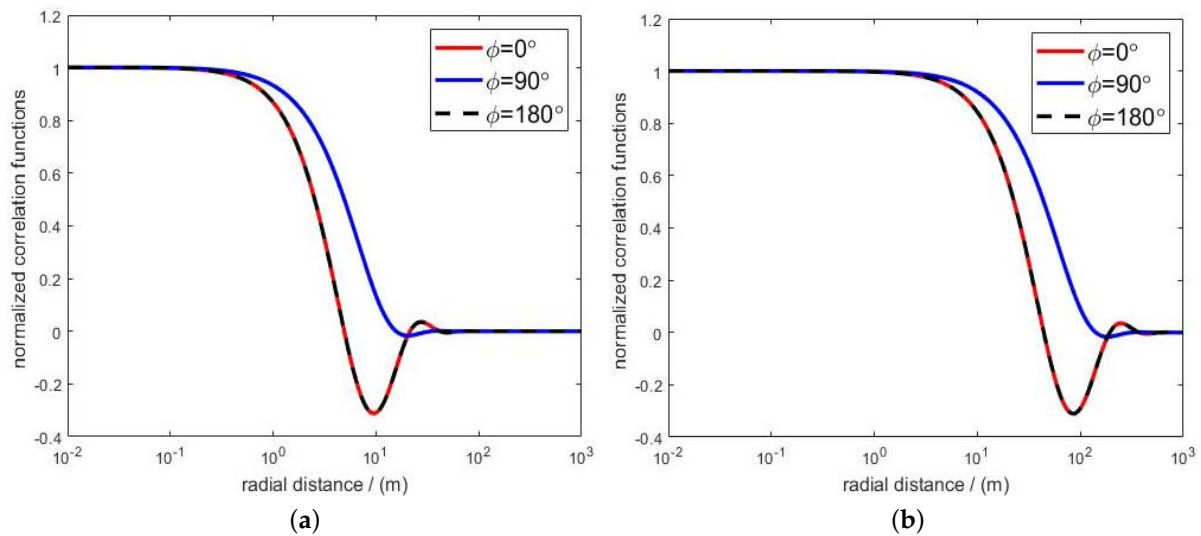


Figure 4. Normalized correlation functions for different ocean wind. (a) $U_{10} = 5$ m/s. (b) $U_{10} = 15$ m/s.

For non-Gaussian seas, the widely used slope distribution function is the Gram–Charlier distribution, developed by Cox and Munk [40]. It can accurately describe a rough sea surface with a relatively small slope. Without considering the interaction between the slope components, the sea surface slope can be expanded using the Gram–Charlier series, which by simplification gives the fourth order Gram–Charlier distribution function as:

$$\begin{aligned}
 p(\zeta_x, \zeta_y) = & \frac{1}{2\pi\sigma_{sx}\sigma_{sy}} \exp\left(-\frac{1}{2}\left(\frac{\zeta_x^2}{\sigma_{sx}^2} + \frac{\zeta_y^2}{\sigma_{sy}^2}\right)\right) \\
 & \left[1 - \frac{1}{2}c_{12}\frac{\zeta_x}{\sigma_{sx}}\left(\frac{\zeta_y^2}{\sigma_{sy}^2} - 1\right) - \frac{1}{6}c_{30}\left(\frac{\zeta_x^3}{\sigma_{sx}^3} - 3\frac{\zeta_x}{\sigma_{sx}}\right) + \frac{1}{24}c_{40}\left(\frac{\zeta_x^4}{\sigma_{sx}^4} - 6\frac{\zeta_x^2}{\sigma_{sx}^2} + 3\right) \right] \\
 & \left[+ \frac{1}{4}c_{22}\left(\frac{\zeta_x^2}{\sigma_{sx}^2} - 1\right)\left(\frac{\zeta_y^2}{\sigma_{sy}^2} - 1\right) + \frac{1}{24}c_{04}\left(\frac{\zeta_y^4}{\sigma_{sy}^4} - 6\frac{\zeta_y^2}{\sigma_{sy}^2} + 3\right) \right] \quad (22)
 \end{aligned}$$

where ζ_x and ζ_y is indicates the slope in the upwind and crosswind directions, respectively. σ_{sx}^2 and σ_{sy}^2 are their variances. The constant factor c_{30} and c_{12} characterizes the skewness, c_{40} , c_{04} and c_{22} characterizes the kurtosis. When describing the clean sea surface, we obtain:

$$\begin{cases} c_{12} = 0.01 - 0.86 \times 10^{-2}U_{12} \pm 0.03 \\ c_{30} = 0.04 - 3.3 \times 10^{-2}U_{12} \pm 0.12 \end{cases} \quad (23)$$

$$\begin{cases} c_{04} = 0.4 \pm 0.23 \\ c_{22} = 0.12 \pm 0.06 \\ c_{40} = 0.23 \pm 0.41 \end{cases} \quad (24)$$

where $U_{12} \approx U_{10}$, error about 2%.

From Equations (15) and (22), Bourlier derived an approximate expression for third- and fourth-order statistical moments based on the characteristic function of the slopes. They can then be simplified as [45]:

$$W_3(r, \phi) = W_{30}(r) \cos(\phi) \quad (25)$$

$$W_{30}(r) = -\sigma_{zs}^3 \frac{r^3}{L_{c3}^3} \exp\left(-\frac{r^2}{L_{c3}^2}\right) \quad (26)$$

$$W_{4d}(r) = \sigma_{zl}^4 \frac{r^4}{L_{c4}^4} \exp\left(-\frac{r^4}{L_{c4}^4}\right) \tag{27}$$

with

$$L_{c3} = \left(\frac{6}{c_{03}}\right)^{1/3} \frac{\sigma_{zs}}{\sigma_{sx}} \tag{28}$$

$$L_{c4} = \sigma_{zl} \left(\frac{2}{\sigma_{sx}\sigma_{sy}\sqrt{c_{22}}}\right)^{1/2} \tag{29}$$

where L_{c3} and L_{c4} are the correlation lengths of the skewness and deviated peakedness factors, respectively. σ_{zs} and σ_{zl} means small- and large-scale root mean square for rough ocean surface $\sigma_z^2 = \sigma_{zs}^2 + \sigma_{zl}^2$, which are related to skewness and peakedness, respectively. The cutoff wavenumber K_c can separate the small- and the large- scales. This once again emphasizes the need for cutoff wavenumber determination. $(\sigma_{sx}^2, \sigma_{sy}^2)$ are the mean square slope in the up- and cross-wind directions, and we have following:

$$\begin{cases} \sigma_{sx}^2 = \int_0^\infty \int_0^{2\pi} k^2 \cdot W(k, \varphi) \cdot \cos^2 \varphi \cdot dk d\varphi \\ \sigma_{sy}^2 = \int_0^\infty \int_0^{2\pi} k^2 \cdot W(k, \varphi) \cdot \sin^2 \varphi \cdot dk d\varphi \end{cases} \tag{30}$$

In Figure 5, the variation of the normalized correlation functions of the height, the skewness, and the deviated peakedness with radial distance for different wind speeds is shown. Note that the radial distance of the skewness decreases as the wind speed becomes higher, which is in contrast to the trend of the mean square height and deviated peakedness. This is because the variation in skewness is determined by small scale capillary waves, a part that is insensitive to the L-band, while mean square height and deviated peakedness are associated with large scale gravity waves, as is clearly demonstrated by Equations (16), (28), and (29).

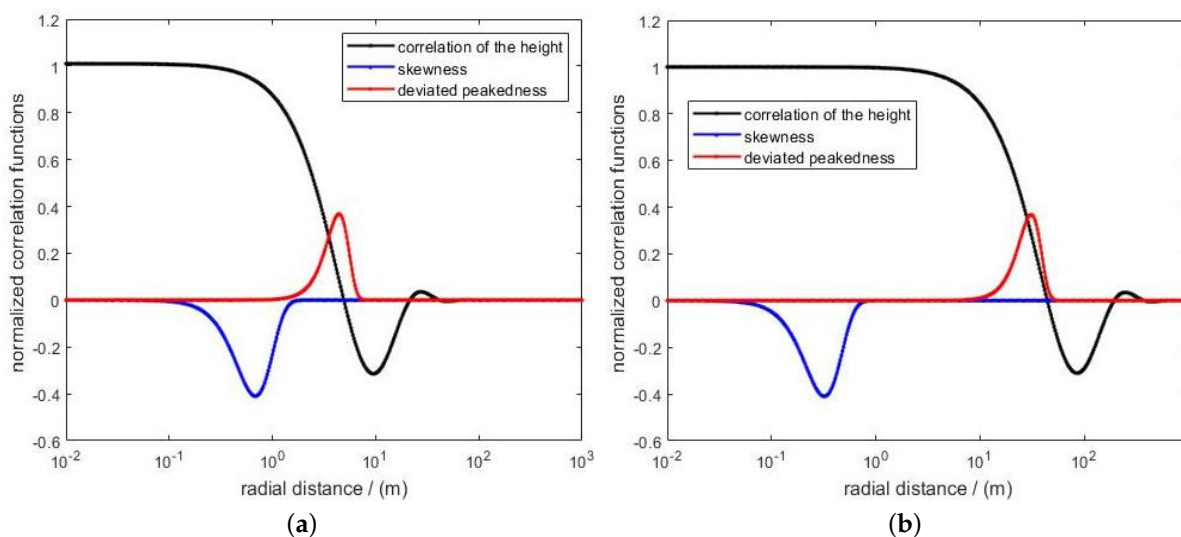


Figure 5. Comparison of skewness, deviated peakedness, and normalized correlation functions of height for $\phi = 0^\circ$ and for different wind speed. (a) $U_{10} = 5$ m/s. (b) $U_{10} = 15$ m/s.

3.3. L-Band Forward Scattering Coefficient

Substituting Equations (25)–(27) into (15), we have:

$$\begin{aligned} \sigma_{pq p' q'}^0(\bar{k}_i, \bar{k}_s) &= \frac{1}{\pi} \left| \frac{2q_i q_s}{q_i + q_s} \right|^2 B_{pq}(\bar{k}_i, \bar{k}_s) B_{p' q'}(\bar{k}_i, \bar{k}_s) \exp\left[-(q_i + q_s)^2 \sigma_z^2\right] \\ &\cdot \int_0^\infty r dr \int_0^{2\pi} \exp[ik_{si} r \cos(\phi - \varphi)] \\ &\cdot \left\{ \exp\left[(q_i + q_s)^2 W_2 + i(q_i + q_s)^3 W_3 + (q_i + q_s)^4 \frac{W_{4d}}{2}\right] - 1 \right\} d\phi \end{aligned} \quad (31)$$

with

$$k_{si} = \sqrt{(k_{sx} - k_{ix})^2 + (k_{sy} - k_{iy})^2} \quad (32)$$

$$k_{sx} = K \sin \theta_s \cos \varphi_s \quad k_{sy} = K \sin \theta_s \sin \varphi_s \quad (33)$$

$$k_{ix} = K \sin \theta_i \cos \varphi_i \quad k_{iy} = K \sin \theta_i \sin \varphi_i \quad (34)$$

This integral is a complex operation that contains a real part related to the correlation functions of height and deviated peakedness and an imaginary part determined by the skewness. This result is consistent with Ref. [44], where the asymmetry caused by the wind direction is influenced by the imaginary part determined by the skewness $\exp(i(q_i + q_s)^3 W_3)$, but in purely specular scattering, $k_{si} \approx 0$, $\exp[ik_{si} r \cos(\phi - \varphi)] = \cos(k_{si} r \cos(\phi - \varphi)) + i \sin(k_{si} r \cos(\phi - \varphi))$, $\sin(k_{si} r \cos(\phi - \varphi)) \approx 0$, the effect of skewness is very small, so that even for non-Gaussian sea scatter, the up/downwind remains indistinguishable in specular scattering [45].

Therefore, taking only the real part affected by surface roughness and utilizing the Bessel function, Equation (31) can be simplified as:

$$\begin{aligned} \sigma_{pq p' q'}^0(\bar{k}_i, \bar{k}_s) &= \frac{1}{\pi} \left| \frac{2q_i q_s}{q_i + q_s} \right|^2 B_{pq}(\bar{k}_i, \bar{k}_s) B_{p' q'}(\bar{k}_i, \bar{k}_s) \exp\left[-(q_i + q_s)^2 \sigma_z^2\right] \\ &\cdot \int_0^\infty \left\{ \exp\left[(q_i + q_s)^2 W_2 + i(q_i + q_s)^3 W_3 + (q_i + q_s)^4 \frac{W_{4d}}{2}\right] - 1 \right\} J_0(k_{si} r) r dr \end{aligned} \quad (35)$$

4. Results

In this section, based on the non-Gaussian ocean surface scattering model above, the fully polarization BRCS of the right-hand circular polarization signal incident on the ocean surface in the L-band is simulated in combination with GNSS-R geometrical properties.

4.1. The Effect of Observation Angle on BRCS

According to the geometry of Figure 1, there are four influential parameters in terms of the angle of observation. The plane of incidence is generally taken as the reference $\varphi_i = 0$. Thus, geometry angle applied to GNSS-R is $\theta_i = \theta_s$, $\varphi_i = \varphi_s = 0$. In Figure 6, we have the effect on the BRCS caused by changes in the incidence angle for different wind speeds. We note that the non-Gaussian NBRCS is a little larger than the Gaussian NBRCS, due to the effect of peakedness correction. Clearly, there are various polarization components in all ranges of incidence angles, and $\sigma_{RH}^0 > \sigma_{RL}^0 > \sigma_{RV}^0 > \sigma_{RR}^0$, which is consistent with the performance of the Fresnel reflection coefficient. The amount of correction is the same for all four polarizations, on average around 0.4 dB, as shown in Figure 7, and decreases with the increasing wind speed. In addition, σ_{RL}^0 , σ_{RV}^0 and σ_{RH}^0 have a similar trend at the incidence angles $[20^\circ, 40^\circ]$, with just a small difference at larger incidence angles, indicating that they are less sensitive to the incidence angle. This is consistent with the results of the study in the literature [2]. This is due to reflection symmetry, with zero correlation between the co-polarized and cross-polarized channels ($S_{HH} \cdot S_{HV}^* = S_{VV} \cdot S_{HV}^* = 0$). Furthermore, the longer the wavelength, the greater the penetration capacity. For L-band, cross-polarization (VH/HV) has a weaker penetration capacity than co-polarization (HH/VV), and the cross-polarized cross section is generally much lower than co-polarized cross sections [37,50].

However, σ_{RR}^0 is strongly influenced by the incidence angle, and it is low in moderate incidence angles $[30^\circ, 50^\circ]$, which are the reason why GNSS-R signals are not currently received using right-hand circular polarization.

Figure 8 shows the effect of scattering angle on the NBRCS for a fixed angle of incidence. The black dashed line indicates the specular scattering angle. In the specular direction $\phi_s = 0$, the non-Gaussian NBRCS has the same peak effect as the Gaussian NBRCS, both reaching a maximum at the specular scattering angle ($\theta_i = \theta_s$). Note that the main difference relating to polarization is also beyond $\pm 20^\circ$ of the purely specular scattering angle. The main differences lie in the part away from the specular scattering angle, mainly because of the specific weight of the cross-polarization at large scattering angles. This is due to the reflection of a left-handed circularly polarized incident wave from the sea surface, which reverses the main polarized component. Therefore, choosing circularly polarized reception in the purely specular direction has the same effect as linearly polarized reception.

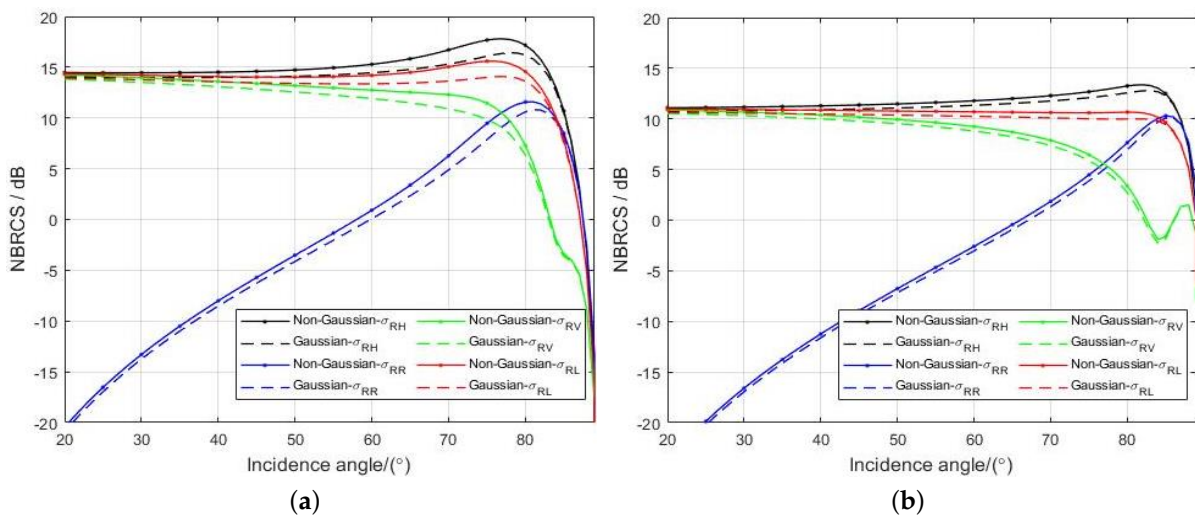


Figure 6. Comparison of fully polarization non-Gaussian NBRCS and Gaussian NBRCS with specular incidence angle θ_i , upwind $\phi = 0^\circ$. (a) $U_{10} = 5$ m/s. (b) $U_{10} = 15$ m/s.

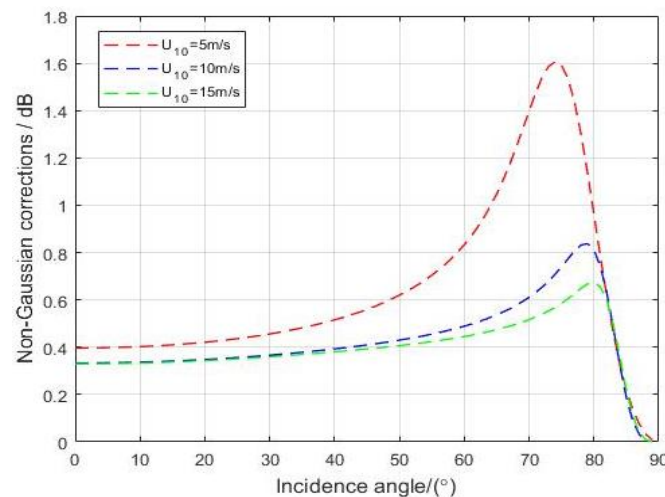


Figure 7. Variation of non-Gaussian correction with incidence angle at different wind speeds.

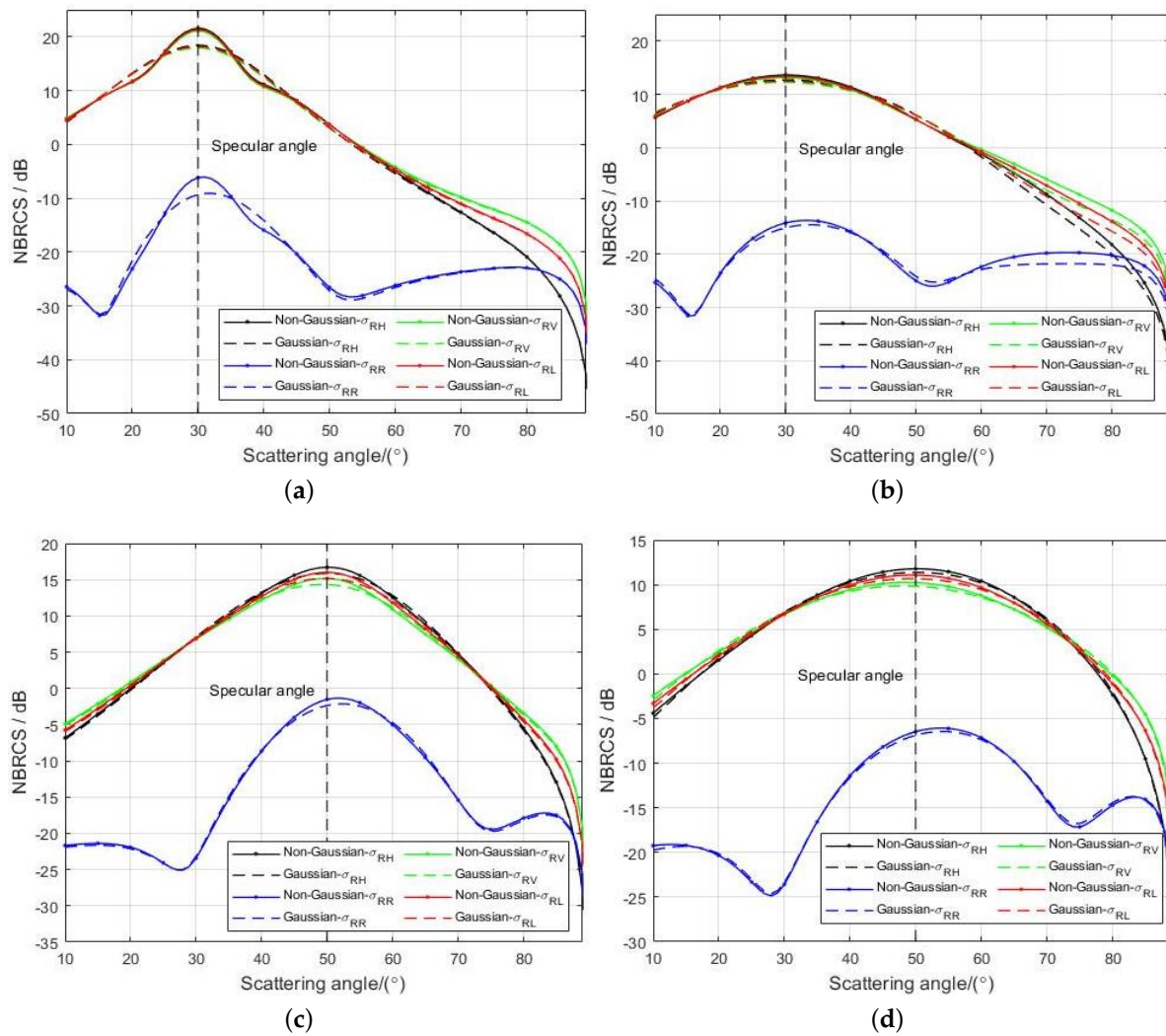


Figure 8. Comparison of fully polarization non-Gaussian BRCS and Gaussian NBRCS with specular incidence angle θ_s . (a) $\theta_i = 30^\circ$, $U_{10} = 5$ m/s, $\phi = 90^\circ$ (b) $\theta_i = 30^\circ$, $U_{10} = 15$ m/s, $\phi = 90^\circ$ (c) $\theta_i = 50^\circ$, $U_{10} = 5$ m/s, $\phi = 0^\circ$ (d) $\theta_i = 50^\circ$, $U_{10} = 15$ m/s, $\phi = 0^\circ$.

Comparing Figure 8a,c and Figure 8b,d, the degree of correction is greater in the cross wind direction. In addition, the amount of NBRCS correction increases as the wind speed increases, which indicates that the peakedness effect of the non-Gaussian correction becomes larger.

4.2. The Effect of Ocean Wind on NBRCS

Under a defined observational geometry, the NBRCS is still mainly influenced by the distribution of the sea surface slope due to the ocean wind.

Due to the non-Gaussian sea surface, the skewness of its distribution is mainly affected by the wind direction. However, according to Figure 9, the NBRCS shows an 'M'-shaped double-peaked structure with the wind direction under the specular scattering geometry, and the non-Gaussian correction only increases the distinguishability between up- and crosswind, and it becomes smaller with the increase of wind speed. At $U_{10} = 15$ m/s, the NBRCS difference between the lateral and downwind directions is less than 3 dB, which is sufficient to indicate a larger area of NBRCS distribution in the low wind speed region during the retrieval, which is consistent with the characteristics in Refs. [2,3,23,55,56]. Furthermore, it does not allow for exact wind detection and still does not solve the problem of up/downwind ambiguity. This is possibly caused by the insensitivity of the skewness

determined by the capillary waves to microwaves in the L-band, which partly determines the skewness of the Gaussian distribution influenced by the wind direction. Because of the analysis in Section 4.1, the polarization behaves similarly under specular scattering geometry, so only the characteristics of circular polarization are analyzed here.

To highlight the necessity for an SSA model, we also used the KA-GO model under a non-Gaussian distribution to simulate the effect of wind direction [57], as shown in Figure 9c, which shows that the NBRCS of the KA-GO model remains independent of wind direction even under non-Gaussian seas, which is consistent with the results in Ref. [46].

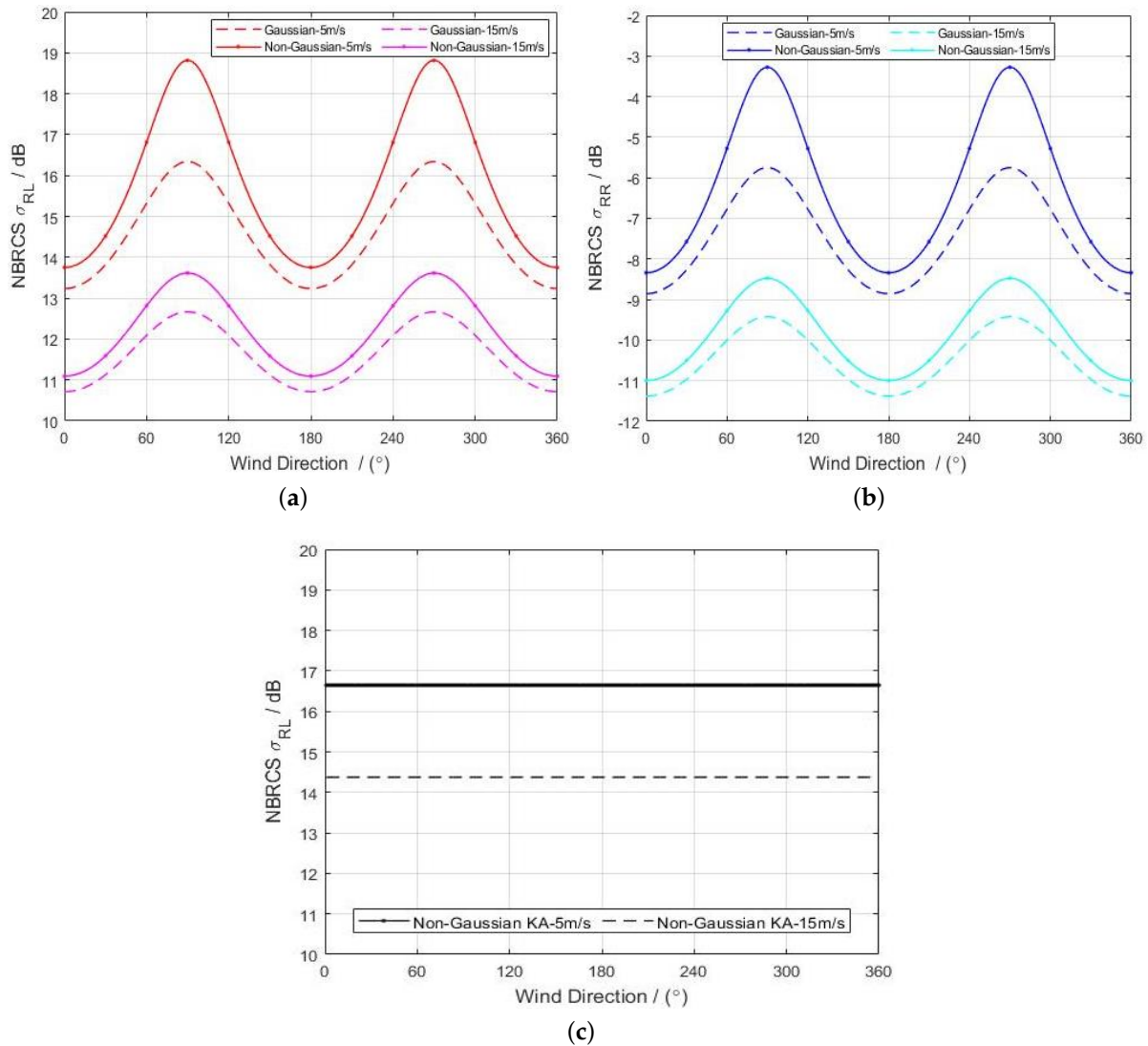


Figure 9. Comparison of non-Gaussian NBRCS and Gaussian NBRCS with wind direction. (a) SSA - σ_{RL}^0 , $\theta_i = \theta_s = 30^\circ$ (b) SSA - σ_{RR}^0 , $\theta_i = \theta_s = 30^\circ$ (c) non-Gaussian KA - σ_{RL}^0 , $\theta_i = \theta_s = 30^\circ$.

However, the variation of NBRCS about wind speed, as shown in Figure 10, has some limitations, and it can be seen that in the low wind speed region, as the wind speed increases, the NBRCS also increases sharply, which is not consistent with the actual scattering situation. This shows that the combined wave spectrum SSA model is unable to effectively simulate the L-band forward scattering from the sea surface at low wind speeds ($U_{10} < 3$ m/s).

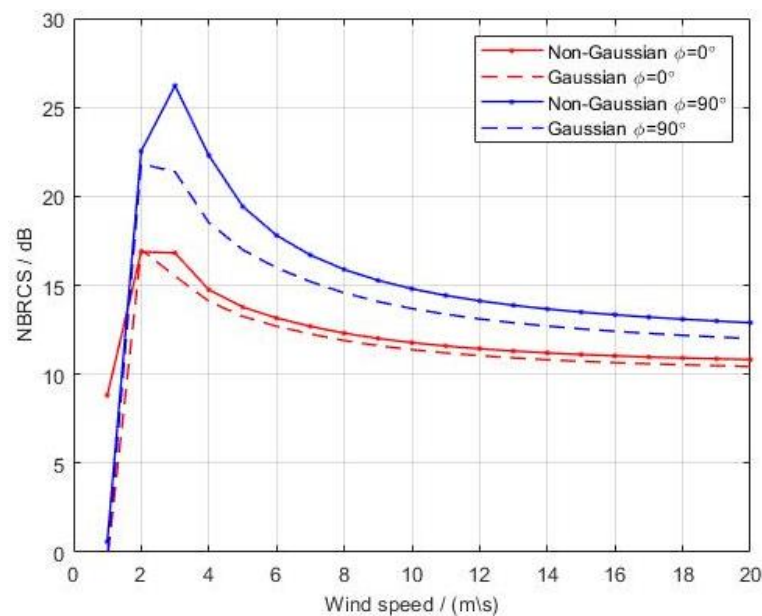


Figure 10. Comparison of non-Gaussian NBRCS and Gaussian NBRCS with wind speed.

To test the accuracy of the model in this paper, we use ECMWF Reanalysis, which includes wind speed and wind direction, and CYGNSS data from 14 September 2018. By temporal-spatial interpolating, the ECMWF Reanalysis data have an interpolated spatial dimension of 0.1° longitude/latitude and 1-min increments of temporal resolution. Then, matching with the quality-controlled CYGNSS data, we can obtain NBRCS with their corresponding wind speed and wind direction [3]. The calculation of NBRCS using L1A data is described in Ref. [58]. Due to the inaccuracy of the model in the low wind speed, we filtered the matching points with wind speed greater than 3 m/s.

Next, the data were filtered for the five wind directions ($\phi = 0^\circ, 30^\circ, 45^\circ, 60^\circ, 90^\circ$), and a functional relationship between NBRCS and ECMWF wind speed is shown in Figure 11. The non-Gaussian SSA model (red solid line) and Gaussian SSA model (red dashed line) were used for comparison, respectively, and it can be seen that there are different detection performances in different wind directions.

In order to verify the performance of the non-Gaussian NBRCS with wind speed, we use the root mean square error (*RMSE*), coefficient (*R*), and the Bias (*Bias*), which are presented in Table 1 and Figure 12.

Table 1. Comparison of *RMSE*, *R*, and *Bias* for non-Gaussian NBRCS with CYGNSS data.

Wind Direction ϕ	<i>RMSE</i>		<i>R</i>		<i>Bias</i>		Number of Matches
	Non-Gaussian SSA	Gaussian SSA	Non-Gaussian SSA	Gaussian SSA	Non-Gaussian SSA	Gaussian SSA	
0°	1.92	2.37	0.60	0.59	-1.68	-2.11	307
30°	1.34	1.73	0.57	0.55	-0.92	-1.44	274
45°	1.22	1.85	0.65	0.64	-0.62	-1.56	362
60°	1.43	1.50	0.66	0.59	0.40	-0.72	326
90°	2.11	1.65	0.72	0.64	1.66	0.43	372
Total	1.60	1.82	0.64	0.60	-0.23	-1.08	1642

Obviously, the non-Gaussian model clearly has a smaller average *RMSE* (1.60 dB) and a smoother trend, with poor accuracy only near the crosswind, and in particular the highest accuracy (1.22 dB) when the wind direction tends to be closer to 45° . However, the non-Gaussian NBRCS is overall low near the upwind and the opposite in the crosswind, which can lead to a necessity to correct the results during the reality check.

Then, correlation analysis was conducted between the model’s estimated NBRCS and CYGNSS data. Figure 13 shows the scatter plot of the estimated NBRCS of non-Gaussian, Gaussian, and the CYGNSS data, respectively. *Bias*, *RMSE*, and R^2 are marked in Figure 13. Non-Gaussian models have better results, the *Bias* is -0.30 dB, the coefficient of determination R^2 is 0.73, and the *RMSE* is 1.81 dB. We can verify that non-Gaussian correction corrects the interval of variation of the NBRCS with ocean wind, and allows for a small bias in the performance of the NBRCS.

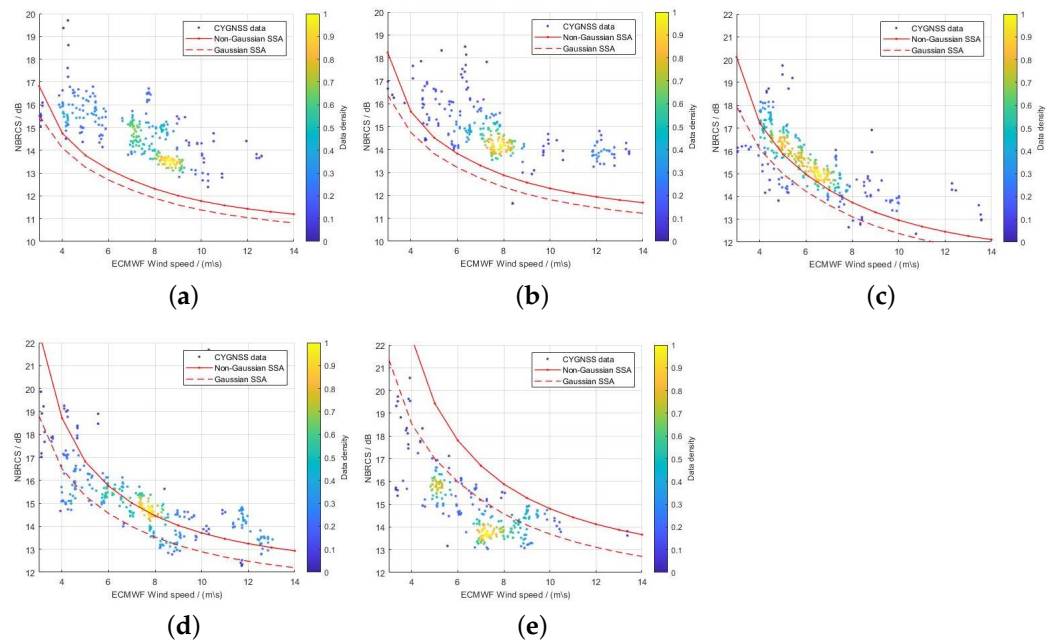


Figure 11. Comparison of non-Gaussian, Gaussian NBRCS, and CYGNSS data for wind speed in different wind direction. The wind direction range is (a) $\phi = 0^\circ$ (b) $\phi = 30^\circ$ (c) $\phi = 45^\circ$ (d) $\phi = 60^\circ$ (e) $\phi = 90^\circ$.

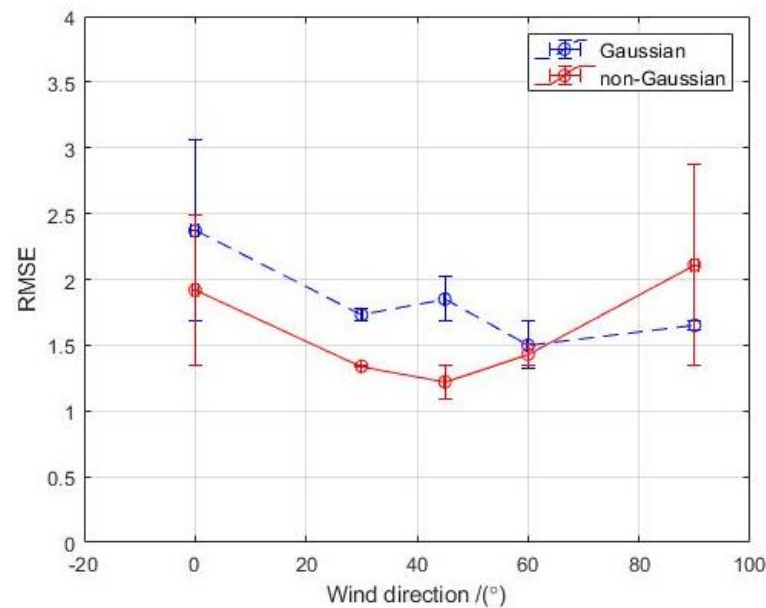


Figure 12. Comparison of *RMSE* and error for non-Gaussian NBRCS with CYGNSS NBRCS.

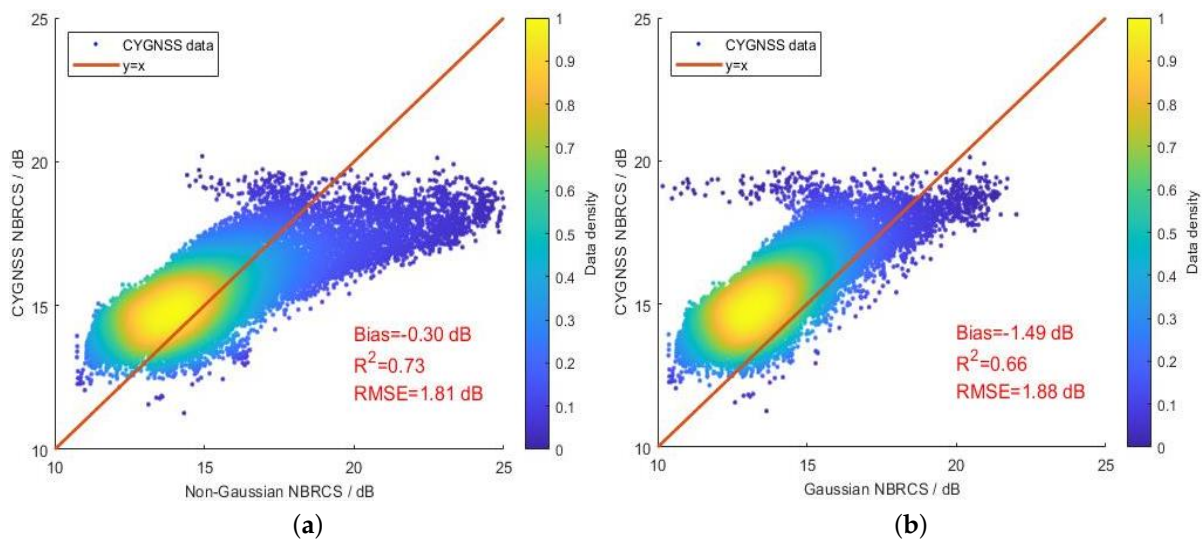


Figure 13. Comparison of non-Gaussian, Gaussian NBRCS, and CYGNSS NBRCS (number of matches = 25,681). (a) Non-Gaussian NBRCS (b) Gaussian NBRCS.

5. Discussion

The non-Gaussian SSA model improves the distinction between up- and crosswind directions, but still fails to accurately invert the wind direction and resolve the ambiguity of the wind direction down/upwind. This is partly due to the observational geometry of the forward specular scattering, and partly due to the insensitivity of the L-band to the larger wavenumber of the sea surface, which affects the skewness factor of the wind direction.

So, if the wind direction is to be distinguished by NBRCS in forward scattering ($\theta_s < 90^\circ$), this also requires deviations from pure specular scattering of the observation structure, and such non-specular NBRCS can theoretically be sought from the DDM away from the specular scattering point.

Selecting several special observation modes, Figure 14 shows the trend of NBRCS with wind direction for an incidence angle of 40° and a wind speed of 10 m/s. The four polarizations have the same variable trend, remaining an 'M'-shaped double-peaked structure with wind direction, but the angle of the peak varies. The non-pure specular observation mode effectively improves its symmetry between up/downwind directions. Comparing Figure 14a,c and Figure 14b,d, we can find that the NBRCS variability is greater for larger scattering angles. In addition, unlike specular scattering, the NBRCS magnitude varies more significantly for different polarizations, as shown in Figures 15 and 16, while what remains constant is that σ_{RH}^0 is always maximum in $\phi_s < 60^\circ$. From the previous analysis, in forward scattering, the HH polarization component is more sensitive to sea surface electromagnetic scattering, especially in the direction away from the pure specular, and the cross-polarization (HV/VH) will also have some effect. Besides, the VV polarization component will reach the scattering Brewster angle more quickly with the change of scattering orientation, as shown in Figure 15, so there are $\sigma_{RL}^0, \sigma_{RV}^0$ about the VV-polarization component are smaller with σ_{RH}^0 [46].

From the above simulations, it can be seen that the scattering azimuth and scattering angle are very important for the final scattering trend in the non-specular observation. These parameters should be taken into account in future studies on wind detection, in addition to which GNSS-R can be extended for applications based on the relative behavior between different polarizations.

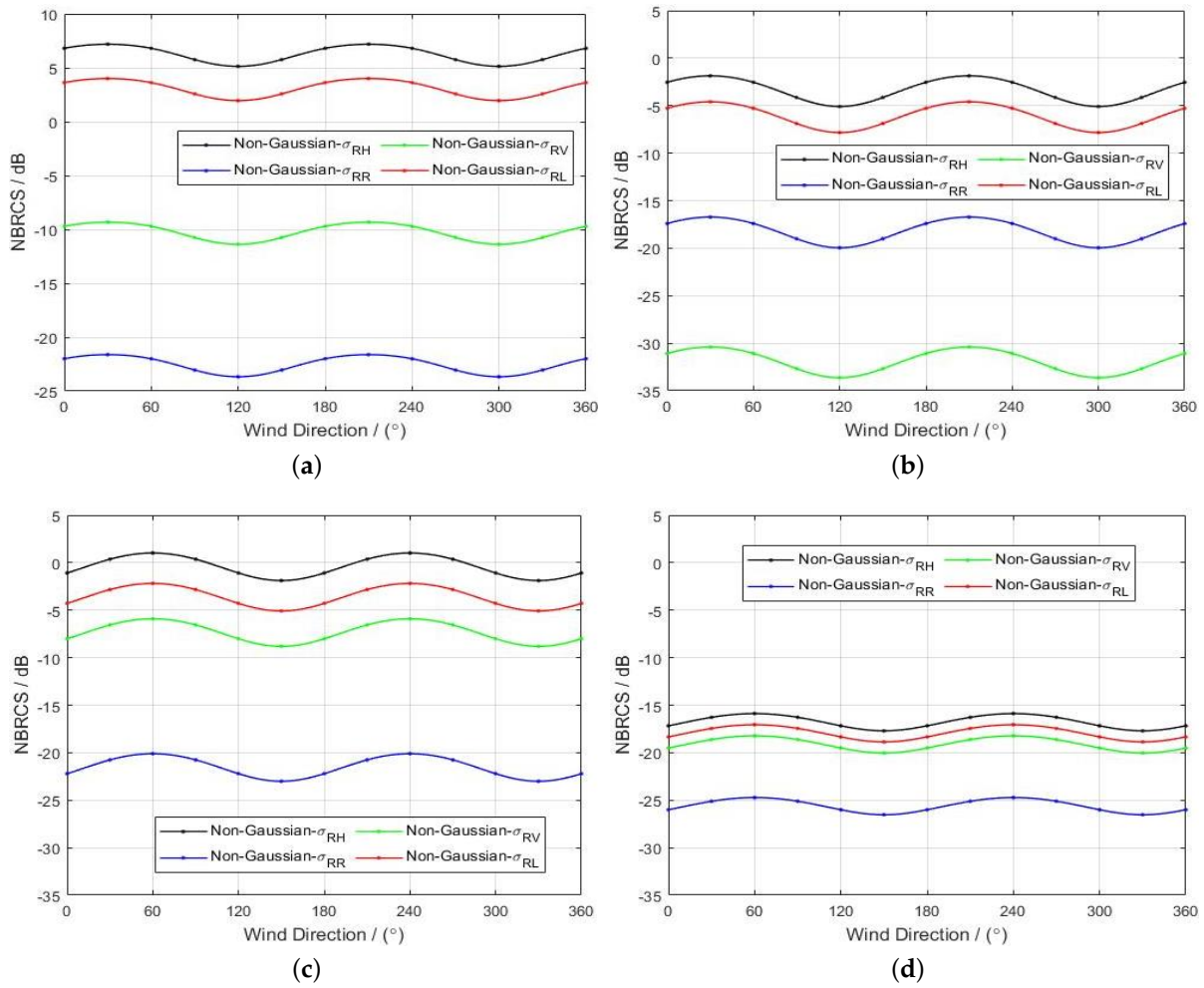


Figure 14. Comparison of fully polarization non-Gaussian BRCS in fully bistatic geometry $\theta_i = 40^\circ$, $U_{10} = 10$ m/s. (a) $\phi_s = 30^\circ$, $\theta_s = 20^\circ$ (b) $\phi_s = 30^\circ$, $\theta_s = 60^\circ$ (c) $\phi_s = 60^\circ$, $\theta_s = 20^\circ$ (d) $\phi_s = 60^\circ$, $\theta_s = 60^\circ$.

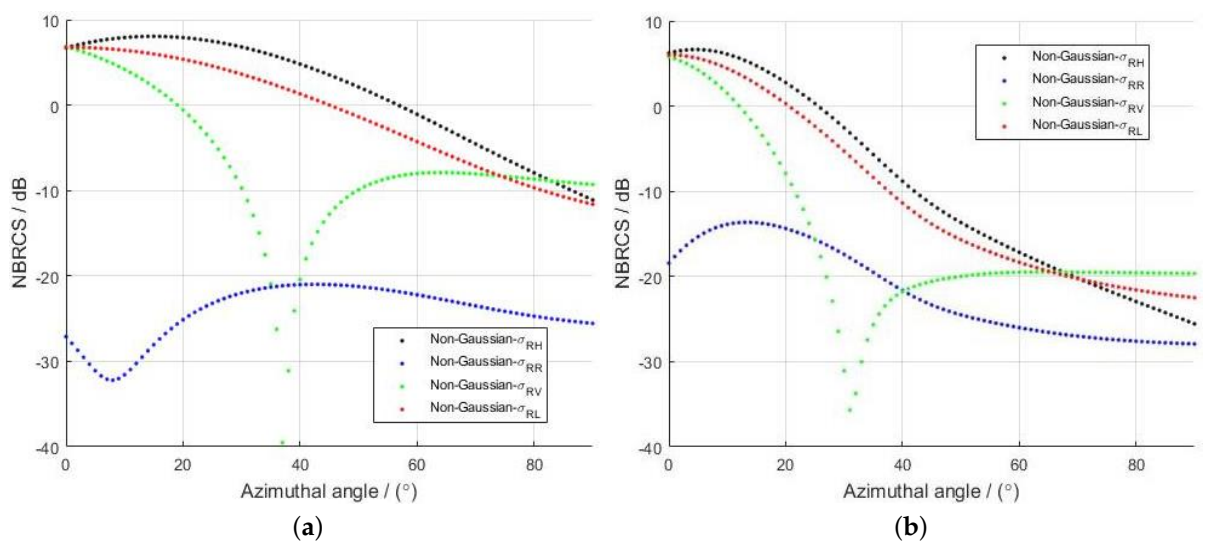


Figure 15. Comparison of non-Gaussian NBRCS in fully bistatic geometry with scattering azimuth angle. $\theta_i = 40^\circ$, $U_{10} = 10$ m/s, $\phi = 0^\circ$. (a) $\theta_s = 20^\circ$ (b) $\theta_s = 60^\circ$.

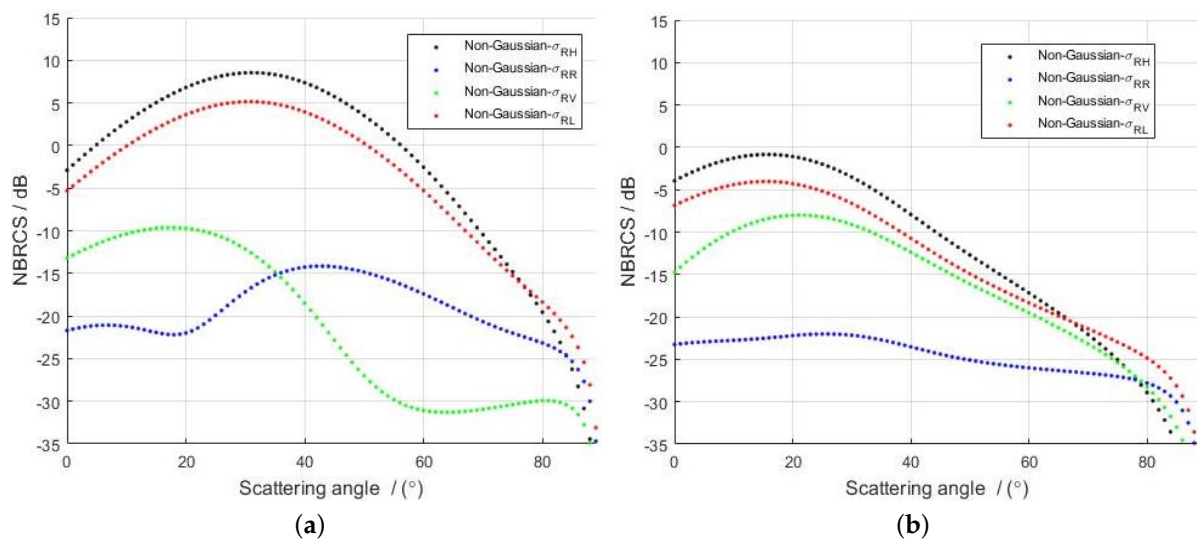


Figure 16. Comparison of non-Gaussian NBRCS in fully bistatic geometry with scattering angle. $\theta_i = 40^\circ$, $U_{10} = 10$ m/s. (a) $\phi_s = 30^\circ$ (b) $\phi_s = 60^\circ$.

6. Conclusions

In this paper, a non-Gaussian small-slope approximation is used to model the forward fully polarized electromagnetic scattering from a bistatic station on a rough ocean surface for GNSS-R, taking into account the properties of the L-band and setting a suitable cut-off wavenumber. In turn, the all-observation geometry and the fully polarized NBRCS characteristics can be effectively analyzed.

For the GNSS right-handed circular polarization incident wave, there is little difference in the performance of σ_{RR}^0 , σ_{RL}^0 , σ_{RH}^0 and σ_{RV}^0 for the fully polarized received mode. In the direction of specular scattering, NBRCS reaches a maximum, and there is always $\sigma_{RH}^0 > \sigma_{RL}^0 > \sigma_{RV}^0 > \sigma_{RR}^0$. Only σ_{RR}^0 is small and very sensitive to the incidence angle.

Due to the consideration of the non-Gaussian properties of the sea surface, both the skewness factor and peakedness factor increase the NBRCS in the pure specular scattering mode of GNSS-R. For non-Gaussian model, the NBRCS increases by about 0.4 dB near the direction of specular scattering, and the extent of this correction becomes more dramatic as the relative wind direction and wind speed become lower.

The non-Gaussian SSA model increases the distinction between the up- and cross-wind, highlighting the variation of NBRCS with wind direction, and the lower the wind speed the more distinguishable it is. However, it still fails to resolve the ambiguity of the down/upwind, which is caused by the insensitivity of the skewness determined by the capillary waves to microwaves in the L-band. Comparing the effects of different wind direction, the non-Gaussian sea surface NBRCS is closer to the results of the CYGNSS real data, which has a smaller average *RMSE* (1.22 dB) and a stable trend. By testing these models, we observed that between the two NBRCS models, the non-Gaussian model have the smallest *Bias* of -0.30 dB, the coefficient of determination R^2 is 0.73, and the *RMSE* is 1.81 dB.

In addition to this, we have analyzed the characteristics of non-specular scattering. The effect of the scattering azimuth and the relative relationship between polarization can be taken into account in future GNSS-R applications.

Author Contributions: W.S. supported the study, processed the data, and wrote the initial draft; X.W. helped with processing the data and writing; W.W. reviewing and editing; B.H. and D.M. supervised the study. All authors have read and agreed to the published version of the manuscript.

Funding: This work was supported by the National Natural Science Foundation of China (Grant No. 62231024, No. 62131019).

Data Availability Statement: Not applicable.

Acknowledgments: The authors are sincerely thankful for the comments from anonymous reviewers and members of the editorial team. Thanks to NASA for providing CYGNSS data products and ECMWF for providing the wind speed and direction products.

Conflicts of Interest: The authors declare no conflict of interest.

References

1. Gleason, S. Space-based GNSS scatterometry: Ocean wind sensing using an empirically calibrated model. *IEEE Trans. Geosci. Remote Sens.* **2013**, *51*, 4853–4863. [[CrossRef](#)]
2. Clarizia, M.P.; Ruf, C.S. Wind speed retrieval algorithm for the Cyclone Global Navigation Satellite System (CYGNSS) mission. *IEEE Trans. Geosci. Remote Sens.* **2016**, *54*, 4419–4432. [[CrossRef](#)]
3. Ruf, C.S.; Balasubramaniam, R. Development of the CYGNSS geophysical model function for wind speed. *IEEE J. Sel. Top. Appl. Earth Obs. Remote Sens.* **2018**, *12*, 66–77. [[CrossRef](#)]
4. Clarizia, M.P.; Ruf, C.S. Statistical derivation of wind speeds from CYGNSS data. *IEEE Trans. Geosci. Remote Sens.* **2020**, *58*, 3955–3964. [[CrossRef](#)]
5. Guo, W.; Du, H.; Cheong, J.W.; Southwell, B.J.; Dempster, A.G. GNSS-R wind speed retrieval of sea surface based on particle swarm optimization algorithm. *IEEE Trans. Geosci. Remote Sens.* **2021**, *60*, 4202414. [[CrossRef](#)]
6. Cardellach, E.; Rius, A. A new technique to sense non-Gaussian features of the sea surface from L-band bi-static GNSS reflections. *Remote Sens. Environ.* **2008**, *112*, 2927–2937. [[CrossRef](#)]
7. Valencia, E.; Zavorotny, V.U.; Akos, D.M.; Camps, A. Using DDM asymmetry metrics for wind direction retrieval from GPS ocean-scattered signals in airborne experiments. *IEEE Trans. Geosci. Remote Sens.* **2013**, *52*, 3924–3936. [[CrossRef](#)]
8. Guan, D.; Park, H.; Camps, A.; Wang, Y.; Onrubia, R.; Querol, J.; Pascual, D. Wind direction signatures in GNSS-R observables from space. *Remote Sens.* **2018**, *10*, 198. [[CrossRef](#)]
9. Zhang, G.; Yang, D.; Yu, Y.; Wang, F. Wind direction retrieval using spaceborne GNSS-R in nonspecular geometry. *IEEE J. Sel. Top. Appl. Earth Obs. Remote Sens.* **2020**, *13*, 649–658. [[CrossRef](#)]
10. Pascual, D.; Clarizia, M.P.; Ruf, C.S. Spaceborne Demonstration of GNSS-R scattering cross section sensitivity to wind direction. *IEEE Geosci. Remote Sens. Lett.* **2021**, *19*, 8006005. [[CrossRef](#)]
11. Li, C.; Huang, W. Sea surface oil slick detection from GNSS-R Delay-Doppler Maps using the spatial integration approach. In Proceedings of the 2013 IEEE Radar Conference (RadarCon13), Ottawa, ON, Canada, 29 April–3 May 2013; pp. 1–6.
12. Li, C.; Huang, W.; Gleason, S. Dual antenna space-based GNSS-R ocean surface mapping: Oil slick and tropical cyclone sensing. *IEEE J. Sel. Top. Appl. Earth Obs. Remote Sens.* **2014**, *8*, 425–435. [[CrossRef](#)]
13. Zhang, Y.; Chen, S.; Hong, Z.; Han, Y.; Li, B.; Yang, S.; Wang, J. Feasibility of oil slick detection using BeiDou-R coastal simulation. *Math. Probl. Eng.* **2017**, *2017*, 8098029. [[CrossRef](#)]
14. Clarizia, M.P.; Ruf, C.; Cipollini, P.; Zuffada, C. First spaceborne observation of sea surface height using GPS-Reflectometry. *Geophys. Res. Lett.* **2016**, *43*, 767–774. [[CrossRef](#)]
15. Cardellach, E.; Li, W.; Rius, A.; Semmling, M.; Wickert, J.; Zus, F.; Ruf, C.S.; Buontempo, C. First precise spaceborne sea surface altimetry with GNSS reflected signals. *IEEE J. Sel. Top. Appl. Earth Obs. Remote Sens.* **2019**, *13*, 102–112. [[CrossRef](#)]
16. Alonso-Arroyo, A.; Zavorotny, V.U.; Camps, A. Sea ice detection using UK TDS-1 GNSS-R data. *IEEE Trans. Geosci. Remote Sens.* **2017**, *55*, 4989–5001. [[CrossRef](#)]
17. Rodriguez-Alvarez, N.; Holt, B.; Jaruwatanadilok, S.; Podest, E.; Cavanaugh, K.C. An Arctic sea ice multi-step classification based on GNSS-R data from the TDS-1 mission. *Remote Sens. Environ.* **2019**, *230*, 111202. [[CrossRef](#)]
18. Li, W.; Cardellach, E.; Fabra, F.; Rius, A.; Ribó, S.; Martín-Neira, M. First spaceborne phase altimetry over sea ice using TechDemoSat-1 GNSS-R signals. *Geophys. Res. Lett.* **2017**, *44*, 8369–8376. [[CrossRef](#)]
19. Mayers, D.; Ruf, C. Measuring ice thickness with CYGNSS altimetry. In Proceedings of the IGARSS 2018—2018 IEEE International Geoscience and Remote Sensing Symposium, Valencia, Spain, 22–27 July 2018; pp. 8535–8538.
20. Unwin, M.; Jales, P.; Tye, J.; Gommenginger, C.; Foti, G.; Rosello, J. Spaceborne GNSS-reflectometry on TechDemoSat-1: Early mission operations and exploitation. *IEEE J. Sel. Top. Appl. Earth Obs. Remote Sens.* **2016**, *9*, 4525–4539. [[CrossRef](#)]
21. Ruf, C.; Chang, P.S.; Clarizia, M.-P.; Gleason, S.; Jelenak, Z.; Majumdar, S.; Morris, M.; Murray, J.; Musko, S.; Posselt, D.; et al. *CYGNSS Handbook*; Michigan Publishing Services: Ann Arbor, MI, USA, 2022.
22. Yang, G.; Bai, W.; Wang, J.; Hu, X.; Zhang, P.; Sun, Y.; Xu, N.; Zhai, X.; Xiao, X.; Xia, J.; et al. FY3E GNOS II GNSS reflectometry: Mission review and first results. *Remote Sens.* **2022**, *14*, 988. [[CrossRef](#)]
23. Foti, G.; Gommenginger, C.; Jales, P.; Unwin, M.; Shaw, A.; Robertson, C.; Rosello, J. Spaceborne GNSS reflectometry for ocean winds: First results from the UK TechDemoSat-1 mission. *Geophys. Res. Lett.* **2015**, *42*, 5435–5441. [[CrossRef](#)]
24. Zavorotny, V.U.; Voronovich, A.G. Scattering of GPS signals from the ocean with wind remote sensing application. *IEEE Trans. Geosci. Remote Sens.* **2000**, *38*, 951–964. [[CrossRef](#)]
25. Zuffada, C.; Elfouhaily, T.; Lowe, S. Sensitivity analysis of wind vector measurements from ocean reflected GPS signals. *Remote Sens. Environ.* **2003**, *88*, 341–350. [[CrossRef](#)]

26. Li, C.; Huang, W. An algorithm for sea-surface wind field retrieval from GNSS-R delay-Doppler map. *IEEE Geosci. Remote Sens. Lett.* **2014**, *11*, 2110–2114.
27. Zavorotny, V.U.; Voronovich, A.G. Recent progress on forward scattering modeling for GNSS reflectometry. In Proceedings of the 2014 IEEE Geoscience and Remote Sensing Symposium, Quebec City, QC, Canada, 13–18 July 2014; pp. 3814–3817.
28. Munoz-Martin, J.F.; Rodriguez-Alvarez, N.; Bosch-Lluis, X.; Oudrhiri, K. Stokes parameters retrieval and calibration of hybrid compact polarimetric GNSS-R signals. *IEEE Trans. Geosci. Remote Sens.* **2022**, *60*, 5113911. [[CrossRef](#)]
29. Munoz-Martin, J.F.; Rodriguez-Alvarez, N.; Bosch-Lluis, X.; Oudrhiri, K. Detection Probability of Polarimetric GNSS-R Signals. *IEEE Geosci. Remote Sens. Lett.* **2023**, *20*, 3500905. [[CrossRef](#)]
30. Zuffada, C.; Fung, A.; Parker, J.; Okolicanyi, M.; Huang, E. Polarization properties of the GPS signal scattered off a wind-driven ocean. *IEEE Trans. Antennas Propag.* **2004**, *52*, 172–188. [[CrossRef](#)]
31. Clarizia, M.P.; Gommenginger, C.; Di Bisceglie, M.; Galdi, C.; Srokosz, M.A. Simulation of L-band bistatic returns from the ocean surface: A facet approach with application to ocean GNSS reflectometry. *IEEE Trans. Geosci. Remote Sens.* **2011**, *50*, 960–971. [[CrossRef](#)]
32. Zavorotny, V.U.; Voronovich, A.G. Bistatic radar scattering from an ocean surface in the small-slope approximation. In Proceedings of the IEEE 1999 International Geoscience and Remote Sensing Symposium. IGARSS'99 (Cat. No. 99CH36293), Hamburg, Germany, 28 June–2 July 1999; Volume 5, pp. 2419–2421.
33. Voronovich, A. Small-slope approximation for electromagnetic wave scattering at a rough interface of two dielectric half-spaces. *Waves Random Media* **1994**, *4*, 337. [[CrossRef](#)]
34. Zavorotny, Z.; Voronovich, A.G.; Katzberg, S.J.; Garrison, J.L.; Komjathy, A. Extraction of sea state and wind speed from reflected GPS signals: Modeling and aircraft measurements. In Proceedings of the IGARSS 2000. IEEE 2000 International Geoscience and Remote Sensing Symposium. Taking the Pulse of the Planet: The Role of Remote Sensing in Managing the Environment. Proceedings (Cat. No. 00CH37120), Honolulu, HI, USA, 24–28 July 2000; Volume 4, pp. 1507–1509.
35. Fung, A.; Tjuatja, S. Backscattering and emission signatures of randomly rough surfaces based on IEM. In Proceedings of the Proceedings of IGARSS'93—IEEE International Geoscience and Remote Sensing Symposium, Tokyo, Japan, 18–21 August 1993; pp. 1006–1008.
36. Awada, A.; Khenchaf, A.; Coatanhay, A. Bistatic radar scattering from an ocean surface at L-band. In Proceedings of the 2006 IEEE Conference on Radar, Verona, NY, USA, 24–27 April 2006.
37. Voronovich, A.G.; Zavorotny, V.U. Full-polarization modeling of monostatic and bistatic radar scattering from a rough sea surface. *IEEE Trans. Antennas Propag.* **2013**, *62*, 1362–1371. [[CrossRef](#)]
38. Elfouhaily, T.; Chapron, B.; Katsaros, K.; Vandemark, D. A unified directional spectrum for long and short wind-driven waves. *J. Geophys. Res. Ocean.* **1997**, *102*, 15781–15796. [[CrossRef](#)]
39. Beckmann, P. Scattering by non-Gaussian surfaces. *IEEE Trans. Antennas Propag.* **1973**, *21*, 169–175. [[CrossRef](#)]
40. Cox, C. Statistics of the sea surface derived from sun glitter. *J. Mar. Res.* **1954**, *13*, 198–227.
41. Longuet-Higgins, M.S. On the skewness of sea-surface slopes. *J. Phys. Oceanogr.* **1982**, *12*, 1283–1291. [[CrossRef](#)]
42. Chapron, B.; Kerbaol, V.; Vandemark, D.; Elfouhaily, T. Importance of peakedness in sea surface slope measurements and applications. *J. Geophys. Res. Ocean.* **2000**, *105*, 17195–17202. [[CrossRef](#)]
43. Nickolaev, N.; Yordanov, O.; Michalev, M. Non-Gaussian effects in the two-scale model for rough surface scattering. *J. Geophys. Res. Ocean.* **1992**, *97*, 15617–15624. [[CrossRef](#)]
44. Chen, K.S.; Fung, A.K.; Weissman, D.A. A backscattering model for ocean surface. *IEEE Trans. Geosci. Remote Sens.* **1992**, *30*, 811–817. [[CrossRef](#)]
45. Bourlier, C. Azimuthal harmonic coefficients of the microwave backscattering from a non-Gaussian ocean surface with the first-order SSA model. *IEEE Trans. Geosci. Remote Sens.* **2004**, *42*, 2600–2611. [[CrossRef](#)]
46. Park, J.; Johnson, J.T. A study of wind direction effects on sea surface specular scattering for GNSS-R applications. *IEEE J. Sel. Top. Appl. Earth Obs. Remote Sens.* **2017**, *10*, 4677–4685. [[CrossRef](#)]
47. Wang, S.; Shi, S.; Ni, B. Joint use of spaceborne microwave sensor data and CYGNSS data to observe tropical cyclones. *Remote Sens.* **2020**, *12*, 3124. [[CrossRef](#)]
48. Cardellach, E.; Nan, Y.; Li, W.; Padullés, R.; Ribó, S.; Rius, A. Variational retrievals of high winds using uncalibrated CyGNSS observables. *Remote Sens.* **2020**, *12*, 3930. [[CrossRef](#)]
49. Saïd, F.; Soisuvann, S.; Jelenak, Z.; Chang, P.S. Performance assessment of simulated CYGNSS measurements in the tropical cyclone environment. *IEEE J. Sel. Top. Appl. Earth Obs. Remote Sens.* **2016**, *9*, 4709–4719. [[CrossRef](#)]
50. Nord, M.E.; Ainsworth, T.L.; Lee, J.S.; Stacy, N.J. Comparison of compact polarimetric synthetic aperture radar modes. *IEEE Trans. Geosci. Remote Sens.* **2008**, *47*, 174–188. [[CrossRef](#)]
51. Voronovich, A.; Zavorotny, V. Theoretical model for scattering of radar signals in K u-and C-bands from a rough sea surface with breaking waves. *Waves Random Media* **2001**, *11*, 247. [[CrossRef](#)]
52. McDaniel, S.T. Small-slope predictions of microwave backscatter from the sea surface. *Waves Random Media* **2001**, *11*, 343. [[CrossRef](#)]
53. Longuet-Higgins, M.S. The effect of non-linearities on statistical distributions in the theory of sea waves. *J. Fluid Mech.* **1963**, *17*, 459–480. [[CrossRef](#)]

54. Thompson, D.R.; Elfouhaily, T.M.; Garrison, J.L. An improved geometrical optics model for bistatic GPS scattering from the ocean surface. *IEEE Trans. Geosci. Remote Sens.* **2005**, *43*, 2810–2821. [[CrossRef](#)]
55. Jing, C.; Niu, X.; Duan, C.; Lu, F.; Di, G.; Yang, X. Sea surface wind speed retrieval from the first Chinese GNSS-R mission: Technique and preliminary results. *Remote Sens.* **2019**, *11*, 3013. [[CrossRef](#)]
56. Ruf, C.S.; Gleason, S.; McKague, D.S. Assessment of CYGNSS wind speed retrieval uncertainty. *IEEE J. Sel. Top. Appl. Earth Obs. Remote Sens.* **2018**, *12*, 87–97. [[CrossRef](#)]
57. Wang, F.; Yang, D.; Yang, L. Feasibility of wind direction observation using low-altitude global navigation satellite system-reflectometry. *IEEE J. Sel. Top. Appl. Earth Obs. Remote Sens.* **2018**, *11*, 5063–5075. [[CrossRef](#)]
58. Gleason, S.; Ruf, C.S.; Clarizia, M.P.; O'Brien, A.J. Calibration and unwrapping of the normalized scattering cross section for the cyclone global navigation satellite system. *IEEE Trans. Geosci. Remote Sens.* **2016**, *54*, 2495–2509. [[CrossRef](#)]

Disclaimer/Publisher's Note: The statements, opinions and data contained in all publications are solely those of the individual author(s) and contributor(s) and not of MDPI and/or the editor(s). MDPI and/or the editor(s) disclaim responsibility for any injury to people or property resulting from any ideas, methods, instructions or products referred to in the content.